

Flow Completion Network: Inferring the Fluid Dynamics from Incomplete Flow Information using Graph Neural Networks

Xiaodong He,¹ Yinan Wang,² and Juan Li³

¹*Department of R&D, UnionString(Beijing) Technology Co. Ltd., Beijing, CHINA.*

²*School of Engineering, University of Liverpool, Liverpool L69 3BX, UK.*

³*Department of Engineering, King's College London, London WC2R 2LS, UK.*

(*Corresponding Author: juan.li@kcl.ac.uk)

(Dated: 11 May 2022)

This paper introduces a novel neural network - the flow completion network (FCN) - to infer the fluid dynamics, including the flow field and the force acting on the body, from the incomplete data based on Graph Convolution Attention Network. The FCN is composed of several graph convolution layers and spatial attention layers. It is designed to infer the velocity field and the vortex force contribution of the flow field when combined with the vortex force map (VFM) method. Compared with other neural networks adopted in fluid dynamics, the FCN is capable of dealing with both structured data and unstructured data. The performance of the proposed FCN is assessed by the computational fluid dynamics (CFD) data on the flow field around a circular cylinder. The force coefficients predicted by our model are validated against those obtained directly from CFD. Moreover, it is shown that our model effectively utilizes the existing flow field information and the gradient information simultaneously, giving a better performance than the traditional CNN-based and DNN-based models.

I. INTRODUCTION

Flow field completion and body force extraction from incomplete known flow field information are important in a range of applications. Examples include one of the key approaches in experimental fluid dynamics - particle image velocimetry (PIV)^{1,2}, where non-invasive force measurements have long been a challenging task. Another application is the load prediction and controls in aeroelastic problems, such as the wind farm flow prediction and control from LIDAR measurements³. The flow field reconstruction from sparse sensors⁴ also involves the flow completion techniques. Solving the Navier-Stokes equations in computational fluid dynamics (CFD) could give the detailed flow field and the pressure distribution and skin friction on the body surface, thus the unsteady force acting on the body. However, high accurate CFD simulation is normally time-consuming and not suitable for a lot of industrial applications, which require quick results. Meanwhile, analytical solutions always have their constraints and few fast calculation methods are available for predicting the flow field and body force. There has been more success with analytical-numerical coupling methods^{5,6}. On the other side, high-precision experimental techniques⁵ make it possible for experimental measurements on fluid dynamic loads. Such direct load measurements can be less accurate and significantly contaminated by resonance effect⁷. Meanwhile, obtaining fluid dynamic loads from an integration of computed surface pressures and skin friction has always been challenging since resolving the entire boundary layer to an adequate resolution near the solid surface is not realistic in most experimental measurements⁷. Thus, volumetric pressure-free methods⁸⁻¹² achieve success in taking advantage of accurate experimental measurements of flow fields such as PIV, and extracting the force on the body in a non-intrusive way. Li and Wu¹³ proposed a vortex force map (VFM) method by further exploring Howe¹¹'s force formula for the derivation of the body force from the vorticity field. The VFM method has been

well extended to a finite and limited chosen region enclosing the body¹⁴ and to three-dimensional flows¹⁵. However, these methods still require detailed flow field information at least in a specific domain enclosing the body. Therefore, in this work, we are going to explore the flow field reconstruction from very limited incomplete measurements and further predict the body force combined with the previously proposed VFM method. Note that the CFD method utilized in this work is purely for providing data and validation purposes.

The recent boom of data-driven approaches and the proliferation of high-quality experimental or CFD flow data have attracted enormous attention in data-driven inference to simulate, reconstruct, incomplete, or predict the fluid dynamics properties. Machine learning has been widely used in reconstruct or the surrogate modeling of the flow fields according to the information collected from either experiments or numerical simulations^{16,17}. Fukami, Fukagata, and Taira¹⁸ adopted a standard convolution neural network (CNN) and developed an improved hybrid Downsampled Skip-Connection Multi-Scale (DSC/MS) model to reconstruct the high-resolution flow field from grossly under-resolved flow field data. They showed a remarkable ability to reconstruct laminar and turbulent flow fields from low-resolution data. Morimoto, Fukami, and Fukagata¹⁹ developed a CNN-based method to estimate the velocity field through imperfect experimental (PIV) measurements of snapshots with missing data. Kochkov *et al.*²⁰ use end-to-end CNN based model to improve approximations inside computational fluid dynamics for modeling two-dimensional turbulent flows. Their research exemplifies how scientific computing can leverage machine learning and hardware accelerators to improve simulations without sacrificing accuracy or generalization. Raissi *et al.*²¹, Raissi, Yazdani, and Karniadakis²² developed a classical physical-informed deep neural network by including the N-S equation in the loss functions to infer the velocity, pressure, and hence the lift and drag from limited and scattered time-space data of the velocity field. This method predicted precisely the flow informa-

tion within the range of the training set. Miyanawala and Jaiman²³ proposed an efficient model reduction technique based on CNN and the stochastic gradient descent method to predict the unsteady fluid dynamic forces for different geometry at low Reynolds numbers. Bhatnagar *et al.*²⁴ built a surrogate model for flow field prediction based on CNN, which was shown to predict the velocity and pressure field orders of magnitude faster than the RANS solver. Specific convolution operations, parameter sharing, and gradient sharpening are used to improve the capability of the CNN.

Most of the traditional CNN-based methods are inherently limited to utilizing structured data since these methods need a generation of a feature matrix that could not apply to unstructured data. Flow measurements are however highly unstructured or even scatter distributed. Moreover, the standard CNN is translation invariant and sensitive to the scale of the data. The resolution of the output data depends on the scale of the training data and the resolution of the input data. In addition, it is difficult to directly use the N-S equation as a loss function in a standard CNN model since CNN-based model structure could not automatically calculate the partial derivative of coordinates through existing deep learning frameworks (such as tensorflow and pytorch).

To perform inference on unstructured or mesh-free data, Trask *et al.*²⁵ introduced GMLS-Nets, which parameterize the generalized moving least-squares functional regression method. The GMLS-Nets demonstrated successful prediction of body forces on a cylinder dataset based on unstructured point cloud fluid data. Ogoke *et al.*²⁶ proposed a data-driven graph neural network (GNN) framework, extended from GraphSAGE²⁷, for the drag force prediction of flow field from irregular and unstructured data. In Hamilton, Ying, and Leskovec²⁷'s work, Top-K pooling step is used to replace the feature aggregation in Hamilton, Ying, and Leskovec²⁷. Whereas, non of these existing GNN-based models apply the laws of physics (NS equations in the fluid dynamics) to the flow field prediction, which is proved to be vital to the accuracy, efficiency, and generalization capability of the model²⁸. Thus, physical-informed GNN applied to unstructured data needs further exploration.

In this work, a novel deep learning model - flow completion network (FCN) - updated from the GraphSAGE²⁷, is designed to accurately predict the velocity field from an incomplete knowledge of the existing flow field data. Combined with the VFM method, the predicted velocity field is directly used to infer the force contribution of the vortex flow field, avoiding the utilization of an intermediate variable - the pressure field. It is well understood that the over-smoothing^{29,30} and the lack of gradient information are detrimental to the convergence rate and the accuracy of the GNN models. Thus, in our FCN, 5 neural net work layers are introduced instead of using a deeper GNN in order to suppress the over-smoothing phenomenon³¹⁻³³. The 5 neural net work layers consist of two graph convolution (GC) layers and three spatial gradient attention (SGA) layers, where the SGA layer could also utilize the gradient information between the reference nodes to perform an accurate information transmission and flow field prediction. Unlike the traditional CNN model which has lim-

ited application in structured data, this model is free from the constraints of data structure and could deal with both structured and unstructured data.

To effectively use the gradient information between nodes, gradient attention layers are carefully designed to facilitate the transmission of gradient information between nodes. This procedure greatly simplifies the structure of the model and increases its performance of the model. Moreover, the N-S equation is integrated into the GNN model training as loss functions, to make sure the obtained model conforms to the physical laws.

The experimental results show that the proposed FCN model could accurately predict the flow features such as the velocity in an efficient manner. It could also predict the body force when combined with the VFM method. It works well on limited or even missing regions of the training data presented on unstructured mesh or scattered points.

In Sec. II, the problem set-up and methodology are introduced. The principle and structure of the proposed flow completion network (FCN) and its sub-modules are described in detail here, as well as a brief introduction to other networks for comparison.

In Sec. III, the results for the flow field reconstruction and force prediction through the FCN model described in Section 2 are presented. Extended experiments are also introduced and analyzed in this section. Concluding remarks are given in Section 4.

II. PROBLEM SET-UP AND METHODOLOGY

We start with a classical flow problem around a circular cylinder. The unsteady fluid motion is governed by the incompressible Navier-Stokes equations where the density of the fluid is a constant ρ and viscosity of the fluid is a constant μ . The solid body is denoted by Ω_B bounded by a closed surface S_B . Given scattered measurements of the snapshot data of the flow field, this work aims to infer the fluid dynamics features, such as the velocity field and the body force. Specifically, this work is devoted to accurately predicting the flow field velocity (u_p, v_p) on arbitrary nodes $\mathbf{x}_p = (x_p, y_p)$, from the observable data (u_r, v_r) on a finite number of reference nodes \mathbf{N}_r with coordinates $\mathbf{x}_r = (x_r, y_r)$. Moreover, with the vortex force map (VFM), we can calculate the body forces (lift and drag) from the inferred velocity fields.

To solve the aforementioned problem, firstly, we use \mathcal{M} to represent the model. The model output

$$\hat{\mathbf{h}}_p = \mathcal{M}(\mathbf{h}_r, \mathbf{x}_r, \mathbf{x}_p) \quad (1)$$

is a function of the model inputs: the observed features \mathbf{h}_r , the coordinates \mathbf{x}_r of the reference nodes, and the coordinates \mathbf{x}_p of the prediction nodes. The outputs of the model are the predicted features $\hat{\mathbf{h}}_p = (\hat{u}_p, \hat{v}_p)$ on the target nodes.

Here the subscript r represents the reference nodes while the subscript p represents the prediction nodes. The symbol with a hat, e.g. $\hat{\mathbf{h}}$, represents the predicted features, while the symbol without a hat (\mathbf{h}) represents the ground truth features. Here in this paper, we presume the ground truth features

are the data computed from CFD. In this paper, we deal with two-dimensional (2D) flow field completion cases, where the model is defined as \mathcal{M}_{FCN} . This 2D model could easily be extended to a three-dimensional (3D) model by extending the 2D N-S loss function Eq. (9) to 3D and changing the coordinates of relevant nodes ($X_p, X_{adj}, x_1 \dots x_6$ in Fig 1 (d)) to 3D coordinates. Part of the data are used to train the model and the rest are used to test and evaluate the model. The details of sampling data set are described in Sec. II C.

After obtaining the velocity fields from the incomplete measurements through the aforementioned model \mathcal{M}_{FCN} , we recall the VFM method¹⁵ to extract the lift and drag coefficients on the circular cylinder

$$\begin{cases} C_L = \frac{2}{V_\infty^2 d} \iint_{\Omega} \vec{\Lambda}_L \bullet (u, v) \omega_z d\Omega + \\ \frac{2}{V_\infty Re} (\oint_{l_B} \omega_z d\phi_L + \oint_{l_B} \omega_z \vec{k}_L \bullet d\vec{l}) \\ C_D = \frac{2}{V_\infty^2 d} \iint_{\Omega} \vec{\Lambda}_D \bullet (u, v) \omega_z d\Omega + \\ \frac{2}{V_\infty Re} (\oint_{l_B} \omega_z d\phi_D + \oint_{l_B} \omega_z \vec{k}_D \bullet d\vec{l}) \end{cases} \quad (2)$$

where V_∞ is the free stream velocity, d is the diameter of the circular cylinder, and $\omega_z = v_x - u_y$ is the vorticity. \vec{k}_L and \vec{k}_D are the unit vector in the lift and drag directions respectively. $Re = \frac{\rho V_\infty d}{\mu}$ is the Reynolds number. The vortex force vectors are defined as

$$\begin{cases} \vec{\Lambda}_L = \left(\frac{(x^2 - y^2)d^2}{4(x^2 + y^2)^2}, \frac{xyd^2}{2(x^2 + y^2)^2} \right) \\ \vec{\Lambda}_D = \left(-\frac{xyd^2}{2(x^2 + y^2)^2}, \frac{(x^2 - y^2)d^2}{4(x^2 + y^2)^2} \right) \end{cases}, \quad (3)$$

and the hypothetical potential are defined as

$$\phi_L = \frac{yd^2}{4(x^2 + y^2)}, \phi_D = \frac{xd^2}{4(x^2 + y^2)}. \quad (4)$$

A. The Flow Completion Network

The main framework of the proposed FCN is shown in Fig. 1. The FCN consists of three graph convolution (GC) modules (GC layers I, II, III) and two spatial gradient attention (SGA) modules (SGA layers I, II), as shown in Fig 1 (a). The GC module is mainly used to learn the node features. The details of the structure of each GC module will be introduced in Sec. II A 1. For a more accurate aggregation process, in other words, learning the flow features on the targeting nodes from the neighbor nodes more accurately, the SGA module is extended from the aggregation module in GraphSAGE²⁷. More details could be found in Sec. II A 2. The N-S loss function in Eq. 9 enables the SGA modules to be capable of learning the gradient characteristics in line with the physical laws described by the N-S equations 8.

1. The Graph Convolution (GC) Module

The GC module is introduced from GraphSAGE²⁷. The role of the GC module is to learn the topological structure and

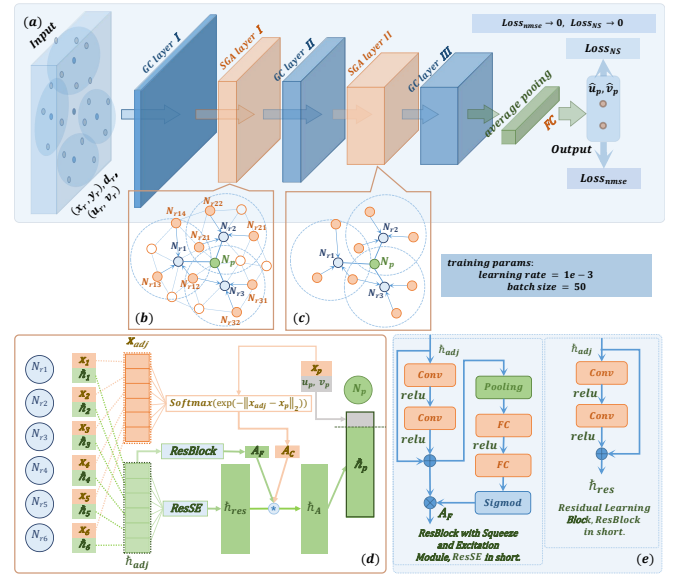


FIG. 1. The structure of the Flow Completion Network (FCN). (a) The framework of the FCN, which consists of an input and an output layer, three graph convolution layers (GC layers I, II, and III), and two spatial gradient attention layers (SGA layers I and II). (b) Visual illustration of the SGA layer I. The reference nodes ($N_{rj1}, N_{rj2}, \dots, N_{rj6}$ shown as solid orange dots) are used to refer the intermediate nodes (N_{rj} shown as solid blue dots). (c) Visual illustration of SGA layer II in (a). Six intermediate nodes ($N_{r1}, N_{r2}, \dots, N_{r6}$) are used to refer the prediction node (N_p shown as solid green dot). Note that, for illustration purpose only, the structure of the GraphSAGE depicted in this figure comprises 3 reference points in each layer. (d) The main framework the SGA layers, which shows how to refer the features on the prediction node N_p from its 6 neighbourhood reference nodes ($N_{r1}, N_{r2}, \dots, N_{r6}$). Here, X_p and \tilde{h}_x are the coordinates and the features of node p , respectively. A_F is features attention, while A_C is coordinates attention. 'ResBlock' represents the Residual Learning Block, and 'ResSE' represents the ResBlock with Squeeze and Excitation Module. (e). The details of the ResBlock and ResSE. 'Conv' denotes the one dimensional convolution layer, 'Pooling' denotes the Global average pooling layer, and 'FC' denotes the full connected layer.

the vertex features, in other words, the embedding representation of vertices. Hamilton, Ying, and Leskovec²⁷ proposed a general, inductive framework that leverages node feature information (e.g., text attributes) to efficiently generate node embedding for the previously unseen data - GraphSAGE. The three GC modules we used is shown in fig.1 (a).

2. The Spatial Gradient Attention Module

In the SGA layers, the spatial-based graph convolution network is introduced, where the GraphSAGE (Graph Sample and aggreGatE) proposed by Hamilton, Ying, and Leskovec²⁷ is adapted here to deal with spatial-based graph. We have made two main aspects of renovations on the original GraphSAGE. The first one is to replace the feature distance layer with the gradient feature attention layer (A_F in Fig. 1 (d)) in

the updated GraphSAGE model. And the second one is to introduce the gradient coordinate attention layer (A_C in Fig. 1 (d)), which is based on spatial coordinate. The two SGA modules (SGA I and SAG II) are shown in fig.1 (b) and (c). Figure 1 (b) shows how to refer the data on the target node N_{ri} from its 6 neighbour nodes $N_{ri1}, N_{ri2}, \dots, N_{ri6}$. For demonstration purposes, only 3 neighbour nodes are depicted in the figure. Similarly, fig.1 (c) shows how to refer the data on the target node N_p from its 6 neighbour nodes $N_{r1}, N_{r2}, \dots, N_{r6}$ and only 3 neighbour nodes are depicted.

The SGA module is proposed here to calculate the spatial gradient and aggregate it into the node features. In order to aggregate node features from multi local neighborhood nodes, We modify the input channel of the attention layers (A_F) from original GraphSAGE frameworks. As shown in figures 1 (d) and (e), the gradient attention layer contains a ResBlock module and a ResSE module. The ResSE is the SE-ResNet Module proposed in Hu *et al.*³⁴, He *et al.*³⁵ and the ResBlock is the Residual module introduced by He *et al.*³⁵.

B. Other Models

As for comparisons to our FCN, *the DNN-based model and the CNN-based model*, commonly used in fluid dynamics, are also introduced here.

a. The DNN-based model $\hat{h}_p = \mathcal{M}_{DNN}(t_p, \mathbf{x}_p)$ relates the input data (time t and the coordinates x) to the predicted features \hat{h}_p on the target nodes. The main framework of \mathcal{M}_{DNN} is shown in Fig. 2 (a). The DNN-based model contains 10 hidden layers, each hidden layer consists of 64 weight neurons and 1 bias neuron. The normal square error loss equation (10) and the Navier-Stokes loss functions are used in the training procedure for our DNN-based model, following the work by Raissi *et al.*²¹.

b. The CNN-based model $\hat{h}_p = \mathcal{M}_{CNN}(\hat{h}_r, m)$ shown in Fig. 2 (b) is similar to the deep learning model proposed by Gao and Grauman³⁶. The input data of the model are the given features \hat{h}_r of the given nodes and the mask m , and the output data is the features \hat{h}_p on the targeting nodes. Here, the mask m is used to distinguish the reference nodes from the target nodes, $m = 0$ refers to the reference node, while $m = 1$ refers to the target node. This model uses a SegNet-like framework³⁷ consisting of encoding layers and decoding layers. Each of the encoding layers contains 4 downsample blocks Down1, Down2, Down3, Down4 as shown in Fig. 2, and each of the decoding layers also contains 4 upsample blocks (Up1, Up2, Up3, Up4) as shown in Fig. 2. A ResBlock³⁵ is used to connect the encoder and the decoder in the CNN-based model. The Mean Square Error loss, same as the loss functions in SegNet³⁷, is used here for the training of the CNN-based model.

C. Dataset, Loss Functions, and Metrics

The flow field data around a circular cylinder obtained by CFD are used as the dataset in this work. We divide the whole

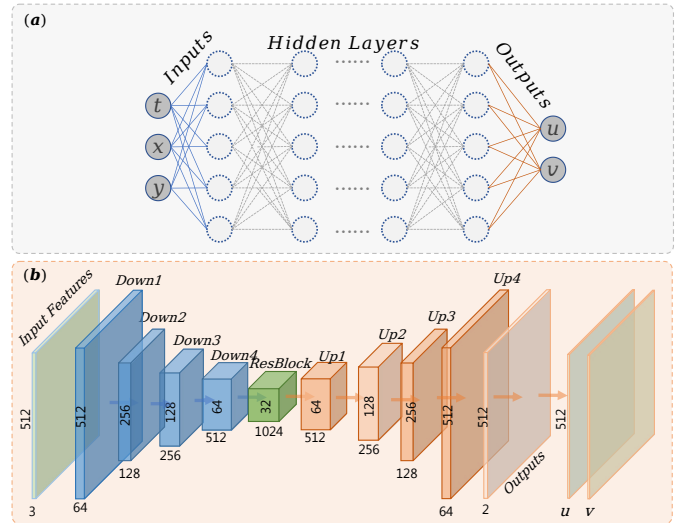


FIG. 2. The main framework of the other models. (a) is the DNN based model \mathcal{M}_{DNN} . The DNN consists of 10 hidden layers and 64 weight neurons and 1 bias neuron per hidden layer. The DNN takes the input variables t , x and y and outputs u and v . (b) is the CNN based model \mathcal{M}_{CNN} .

DataSet	cylinder($Re = 100$)	cylinder($Re = 500$)	cylinder($Re = 1000$)
train	623595/6235950	320950/3209500	400985/4009850
validate	1870785/6235950	962850/3209500	1202955/4009850
test	3741570/6235950	1925700/3209500	2405910/4009850

TABLE I. The detail of the dataset (10% of the total dataset is used as the training set, 30% of the total dataset is used as the validation set, and 60% of the total dataset is used as the test set. The $Re = 100$ cylinder dataset contains 150 snapshots, each snapshot contains 41573 nodes; The $Re = 500$ cylinder dataset contains 50 snapshots, each snapshot contains 64190 nodes; The $Re = 1000$ cylinder dataset contains 50 snapshots, each snapshot contains 80197 nodes.)

dataset into three parts: the training set for the training process of our models; the validation set for finding the proper hyper-parameters, and the test set for assessing the performance of the model. Note that, to ensure the performance of the model in the general cases, there should be no overlap between the training and test datasets. We chose 10%, 30%, 50% of the total data as training sets respectively. To avoid over-fitting, all the metrics for the test set are computed to assess the capability of the model trained by different training data sets. We use u and v as labels in our dataset. And the labels are obtained by CFD. The details of our dataset are listed in table I.

We use the normal mean-square error and the absolute error as the metrics to evaluate the performance of the model. The proportion of the training set is also an important index to measure the generalization ability of the model. If the results of the model are the same, the fewer data used in the model training process, the stronger the generalization ability of the model. $\hat{h}_p = (u_p, v_p)$ is the u and v of the CFD result, \hat{u}_p, \hat{v}_p is predicted u and v for the target nodes by the model \mathcal{M} . The equation of the normal mean-square error E_{nmse} and

the absolute error E_{abs} are defined as

$$E_{nmse}(u) = \frac{\|\widehat{u}_p - u_p\|_2}{\|u_p\|_2}, E_{nmse}(v) = \frac{\|\widehat{v}_p - v_p\|_2}{\|v_p\|_2}, \quad (5)$$

and

$$E_{abs}(u) = |\widehat{u}_p - u_p|, E_{abs}(v) = |\widehat{v}_p - v_p|. \quad (6)$$

To access the generality of the proposed model, in addition to the normal mean-square error of the flow velocity, the absolute error of the force coefficients extracted from the predicted u and v and the coefficients computed by CFD

$$E_{abs}(C_L) = |\widehat{C}_L - C_L|, E_{abs}(C_D) = |\widehat{C}_D - C_D| \quad (7)$$

is also utilized in evaluating the performance of our model.

The motion of fluids is expressed by conservation laws for mass, momentum and energy. The equation for mass is known as the continuity equation while the equation for momentum is called equation of motion that is an expression of Newton's law. If viscous fluid and inviscid fluid are considered in these equations, they are known as the Navier-Stokes and Euler equations, respectively.

Two different loss functions are introduced to the training procedure for our model. One is the NS-equation loss function, another is normal mean square error loss function. Based on the N-S equations

$$\begin{cases} u_t + uu_x + vu_y = -p_x + Re^{-1}(u_{xx} + u_{yy}) \\ v_t + uv_x + vv_y = -p_y + Re^{-1}(v_{xx} + v_{yy}) \\ u_x + v_y = 0 \end{cases}, \quad (8)$$

the N-S loss function could be obtained as

$$\begin{aligned} Loss_{NS}(\widehat{h}_p, \widehat{h}_p, \mathbf{x}_p, Re) = & \|\widehat{u}_x - u_x\|_2 + \|\widehat{u}_y - u_y\|_2 + \\ & Re^{-1} \|\widehat{u}_{xx} - u_{xx}\|_2 + \|\widehat{u}_{yy} - u_{yy}\|_2 + \|\widehat{v}_x - v_x\|_2 + \\ & \|\widehat{v}_y - v_y\|_2 + Re^{-1} \|\widehat{v}_{xx} - v_{xx}\|_2 + \|\widehat{v}_{yy} - v_{yy}\|_2 + \\ & \|\widehat{u}_x + \widehat{v}_y\|_2. \end{aligned} \quad (9)$$

The normal mean square error loss function

$$Loss_{nmse}(\widehat{h}_p, \widehat{h}_p) = \frac{\|u_p - \widehat{u}_p\|_2}{\|u_p\|_2 + \varepsilon} + \frac{\|v_p - \widehat{v}_p\|_2}{\|v_p\|_2 + \varepsilon} \quad (10)$$

is also used in this work. Here, $\varepsilon = 1e - 5$ is added to its denominator to avoid numerical errors. To train the model \mathcal{M}_{FCN} , we aim to minimize the difference between the predicted \widehat{h}_p and the h_p from the CFD result by introducing the loss functions $Loss_{NS}(\widehat{h}_p, \widehat{h}_p, \mathbf{x}_p, Re)$ and $Loss_{nmse}(\widehat{h}_p, \widehat{h}_p)$.

III. EXPERIMENTS AND RESULTS

A. Training

The training dataset mentioned in Sec. II C is used to train different models in our experiments. The Flow Completion Network converges gradually after about 40 epochs of training. The CNN-based model and DNN-based model, used as comparisons here, converge after about 61 and 67 epochs of training, respectively.

1. The Data Augmentation Strategies

In order to improve the generalization of the model, several data augmentation strategies are used during the training procedures. The balance-weight sampling method, gaussian noise method are introduced into our training procedures.

The Balanced Weight Sampling Method. To guide the model to better learn the flow features close to the wall area and predict the flow more accurately, we add the sampling weight $w = 1/(\sqrt{x^2 + y^2} - 0.5 * r)$ to the nodes close to the wall. The nodes closer to the wall have a larger sampling weight, while the nodes farther away from the wall have a smaller sampling weight.

The Gaussian Noise Method. To enhance the fitness of our models, the gaussian noise is added to the original features. The Gaussian noise with zero mean value and 1.0 standard deviation $n_f \sim N(0, 1.0)$ is added to the original features \widehat{h}_r during training procedure.

2. The Hyper-parameters in the Training

The hyper-parameters for the training procedure of our model are shown in the following list:

- Optimizer: SGD;
- Momentum: 0.9;
- Learning rate: 10e-4;
- Batch size:32;
- Training epochs: 100.

The schematics of the unstructured mesh grid used in the CFD simulation and the training data set are shown in Fig. 3. As stated in Sec. 2.3, 10%, 30%, and 50% uniform randomly distributed scatters are subtracted from the total dataset as training datasets. In Fig. 3, we only show the 10% and 30% training dataset for simplicity. Meanwhile, the training data set with and without unobserved regions are also tested.

B. Results

The experimental results on the dataset described in Sec. II C are presented in this section. The proposed FCN model is compared with the traditional CNN and DNN-based models in the same dataset. We also test the generalization ability of all the models on the dataset.

The experiment results of the lift and drag coefficients predicted by the \mathcal{M}_{FCN} , \mathcal{M}_{CNN} , and \mathcal{M}_{DNN} models for different Reynolds numbers are shown in Fig. 4. The non-dimensional time $\tau = tV_\infty/d$. Figures 4 (a) and (b) show that our proposed FCN has a better performance in predicting the lift and drag coefficients than the traditional CNN and DNN-based models. From Fig. 4 (c), we can see that the normalized mean squared error of our proposed model \mathcal{M}_{FCN} is lower than those of \mathcal{M}_{CNN} and \mathcal{M}_{DNN} . Moreover, the performance of the \mathcal{M}_{CNN}

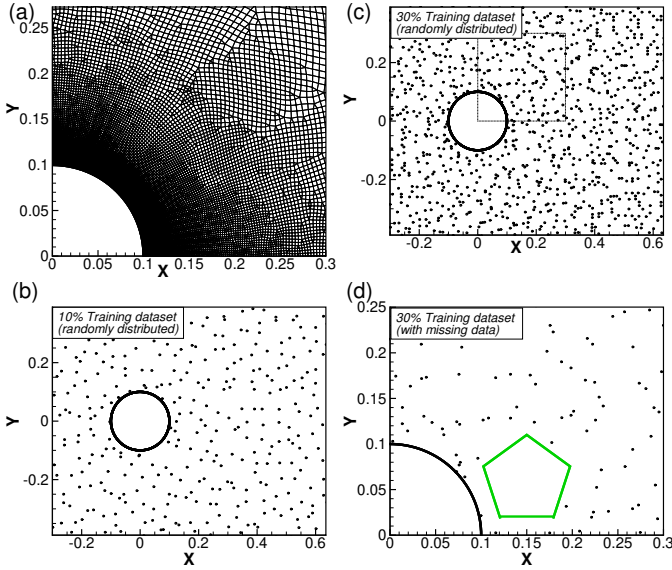


FIG. 3. (a) The schematic of the unstructured mesh grid used in the CFD. (b) The 10% randomly distributed training dataset nodes in the flow field. (c) The 30% randomly distributed training dataset nodes in the flow field without unobserved regions. (d) The 30% randomly distributed training dataset nodes in the flow field with an unobserved pentagonal region in the wake area which is shown in green.

and \mathcal{M}_{DNN} varies with non-dimensional time τ while the proposed \mathcal{M}_{FCN} has a stable performance overall time range. One possible explanation is that our proposed \mathcal{M}_{FCN} could learn physics from the NS loss functions, and utilizes the information on the neighbor nodes, which lead to a better prediction.

The predicted velocity, vorticity, thus lift and drag distribution for the cylinder dataset ($Re = 1000$) obtained from \mathcal{M}_{FCN} and from CFD at a typical instant are shown in Fig. 5. The first two lines of Fig. 5 show the predicted, CFD, and there differences ($Learned - CFD$) on the velocity field ($u(t, x, y)/V_\infty, v(t, x, y)/V_\infty$). The third line of Fig. 5 shows the predicted, CFD, and there differences ($Learned - CFD$) on the vorticity field. While the fourth and fifth lines of Fig. 5 show the predicted, CFD, and there differences ($Learned - CFD$) on the lift and drag distributions respectively. A good comparison has been found between our proposed FCN model and the CFD results.

In order to demonstrate the effectiveness of our \mathcal{M}_{DNN} model, the flow fields completed by our model, the \mathcal{M}_{CNN} model and the \mathcal{M}_{FCN} model are compared with CFD results at different scales, shown in Fig.6. The vorticity ω is demonstrated here. From Fig. 6 we can see that the CNN and DNN-based model learned vorticity field is noisy due to a lack of the second-order gradient information during the training procedure. Our proposed FCN defeats the traditional CNN and DNN-based models regarding the flow field prediction from unstructured data.

It is very common to have shadows or unobserved data in the experimental measurements or point-could represented data. The unobserved data may lie in any arbitrary training

Training	$\mathcal{M}_{CNN}(\text{test/train})$	$\mathcal{M}_{DNN}(\text{test/train})$	$\mathcal{M}_{FCN}(\text{test/train})$
10%	0.7879/0.4934	0.3704/0.2298	0.0546/0.0837
30%	0.6054/0.4787	0.2623/0.2201	0.0552/0.0793
50%	0.5002/0.4370	0.2389/0.1930	0.0540/0.0751

TABLE II. The metrics ($E_{nmse}(u) + E_{nmse}(v)$) of training dataset and testing dataset for \mathcal{M}_{CNN} , \mathcal{M}_{DNN} and \mathcal{M}_{FCN} trained by 10%, 30% and 50% cylinder dataset ($Re = 1000$).

domains which could contain important information. Here in this work, we use a pentagonal region in the wake of the cylinder as an example. The performance of our proposed \mathcal{M}_{FCN} model compared with \mathcal{M}_{DNN} , and \mathcal{M}_{CNN} model with this missing pentagonal region is also tested. The results are shown in Fig. 7, where we could see that the \mathcal{M}_{FCN} completion compares well with the CFD results, while the other two traditional models are not as good.

Fig. 8 shows the training loss and testing loss during the training procedure for the \mathcal{M}_{FCN} , the \mathcal{M}_{CNN} , and the \mathcal{M}_{DNN} , respectively. Fig. 8 (a) shows that the FCN model converges after about 40 epochs of training. The average training loss converges to 0.0806, and the average testing loss converges to 0.1092 which is very close to the average training loss. The gap between the average testing loss and the average training loss indicates that there is no over-fitting during the training procedure of the proposed FCN model. Similarly, in Fig. 8 (b) and (c), the training loss and testing loss are shown to converge after about 61 and 67 epochs of training, respectively. The average training loss and testing loss for the CNN-based model converge to 0.1042 and 0.2324 respectively. The average training loss and testing loss for the DNN-based model converge to 0.0639 and 0.1031 respectively. The convergence rate for the FCN model is the highest among all the models tested here.

The Tab. II list the metrics of training dataset and testing dataset for \mathcal{M}_{CNN} , \mathcal{M}_{DNN} and \mathcal{M}_{FCN} trained by 10%, 30% and 50% cylinder dataset ($Re = 1000$). Trained by 10% dataset, the training dataset metric ($E_{nmse}(u) + E_{nmse}(v)$) for \mathcal{M}_{CNN} is 0.4934, the testing dataset metric for \mathcal{M}_{CNN} is 0.7879, the according metrics for \mathcal{M}_{FCN} is 0.0837 and 0.0546, which indicates the over fitting of \mathcal{M}_{CNN} is more serious than \mathcal{M}_{FCN} in a 10% training dataset. By comparing the metrics of \mathcal{M}_{CNN} , \mathcal{M}_{DNN} and \mathcal{M}_{FCN} trained by 10%, 30% and 50% training dataset, we find that with the reduction of training datasets, the gap between \mathcal{M}_{CNN} and \mathcal{M}_{DNN} training dataset E_{nmse} and testing dataset E_{nmse} is becoming larger and larger, which means that the \mathcal{M}_{CNN} and \mathcal{M}_{DNN} performance is related to the size of training datasets, while our model is much less affected by the size of training dataset.

In order to demonstrate the fitness/generalizability of the proposed FCN model, three observation points (A, B, and C) are selected from the cylinder flow field at $Re = 1000$ (see Fig. 9 (a)) to check the variation of predicted flow features (velocity) against time. The comparison of the velocity variation against time obtained from the FCN model and extracted directly from the CFD is shown in Fig. 9 (b). It is shown that the velocity variation predicted by the proposed FCN model

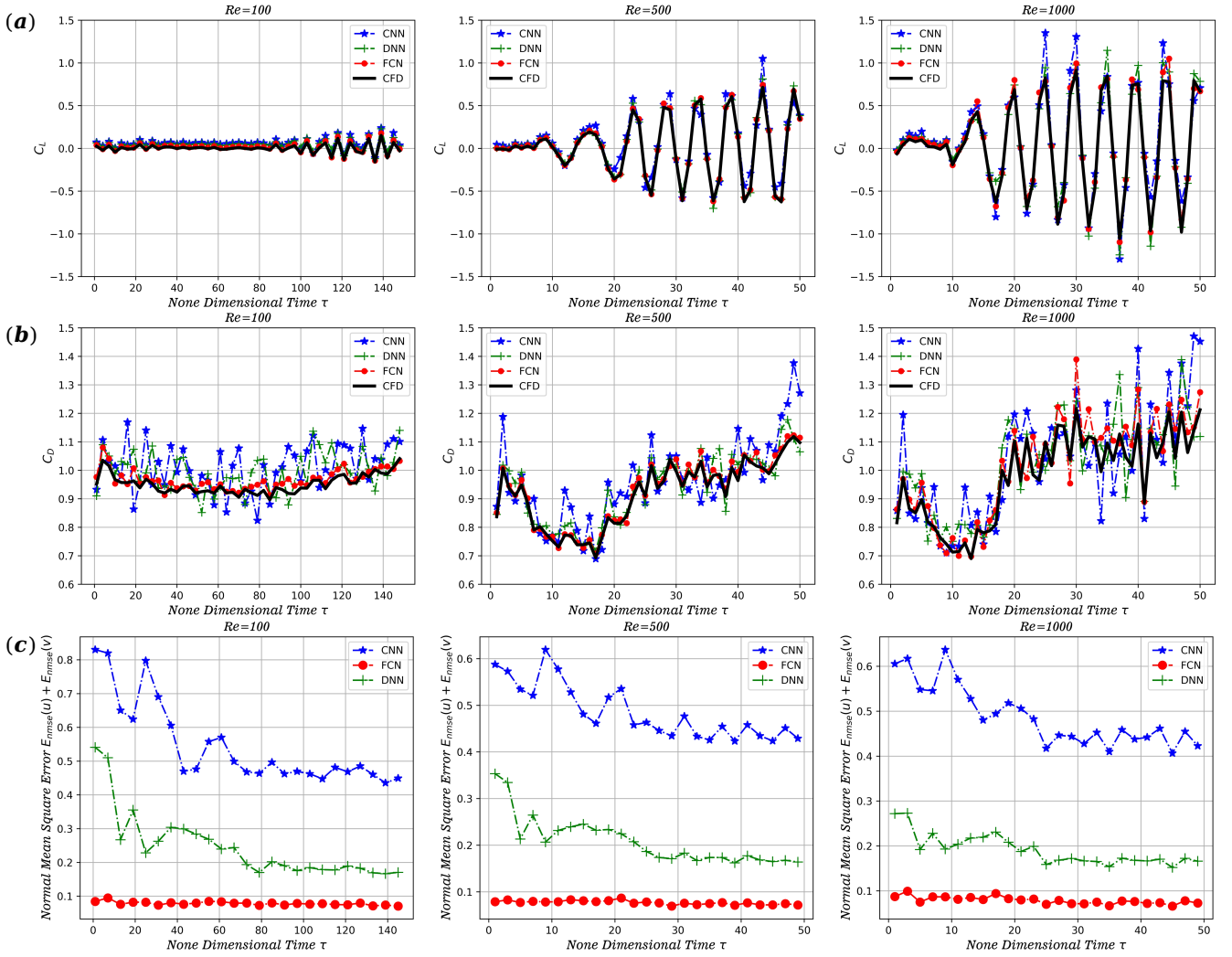


FIG. 4. (a) The comparison of the lift coefficient curve predicted by \mathcal{M}_{FCN} , \mathcal{M}_{CNN} , \mathcal{M}_{DNN} , and computed from the CFD data at three different Reynold numbers: $Re = 100$, $Re = 500$, and $Re = 1000$. (b) The comparison of the drag coefficient curve predicted by \mathcal{M}_{FCN} , \mathcal{M}_{CNN} , \mathcal{M}_{DNN} , and computed from the CFD data at three different Reynold numbers: $Re = 100$, $Re = 500$, and $Re = 1000$. (c) The comparison of the normal mean square error for \mathcal{M}_{FCN} , \mathcal{M}_{CNN} and \mathcal{M}_{DNN} .

compares well with the CFD data, and it has a strong generalization ability. Moreover, the error of the \mathcal{M}_{FCN} does not vary with both the location of the observation point and the time.

IV. CONCLUSION

In this work, we introduced a novel model \mathcal{M}_{FCN} based on GraphSAGE for the flow field completion through using unstructured scattered data. The \mathcal{M}_{FCN} was well designed to contain two GC layers and three SGA layers. The GC layers were introduced to take advantage of the properties of graph convolution neural networks, such as the internal physical law of the flow field (N-S equations). And the SGA layers were introduced to include the spatial gradient information while dealing with unstructured data. As we know, the experimental measurements of the flow field properties are usually

conducted on sparsely scattered points, leading to unstructured data that are difficult to process with traditional machine learning algorithms (e.g. CNN-based models).

To test the proposed FCN model, CFD simulation of a two-dimensional circular cylinder flow at different Reynolds numbers ($Re = 100$, $Re = 500$, $Re = 1000$) on the unstructured mesh was conducted here to provide training data set. The CFD results also served as the 'ground truth'. The absolute error of the lift and drag coefficients, as well as the normal mean square error of the two velocity components, were introduced to evaluate the performance of the proposed FCN model. 10%, 30%, and 50% uniform randomly distributed scatter subtracted from the total dataset with and without unobserved regions have been used as training datasets. The comparison of experimental results from our proposed model together with two other traditional CNN and DNN-based models with CFD 'ground truth' showed the superior-

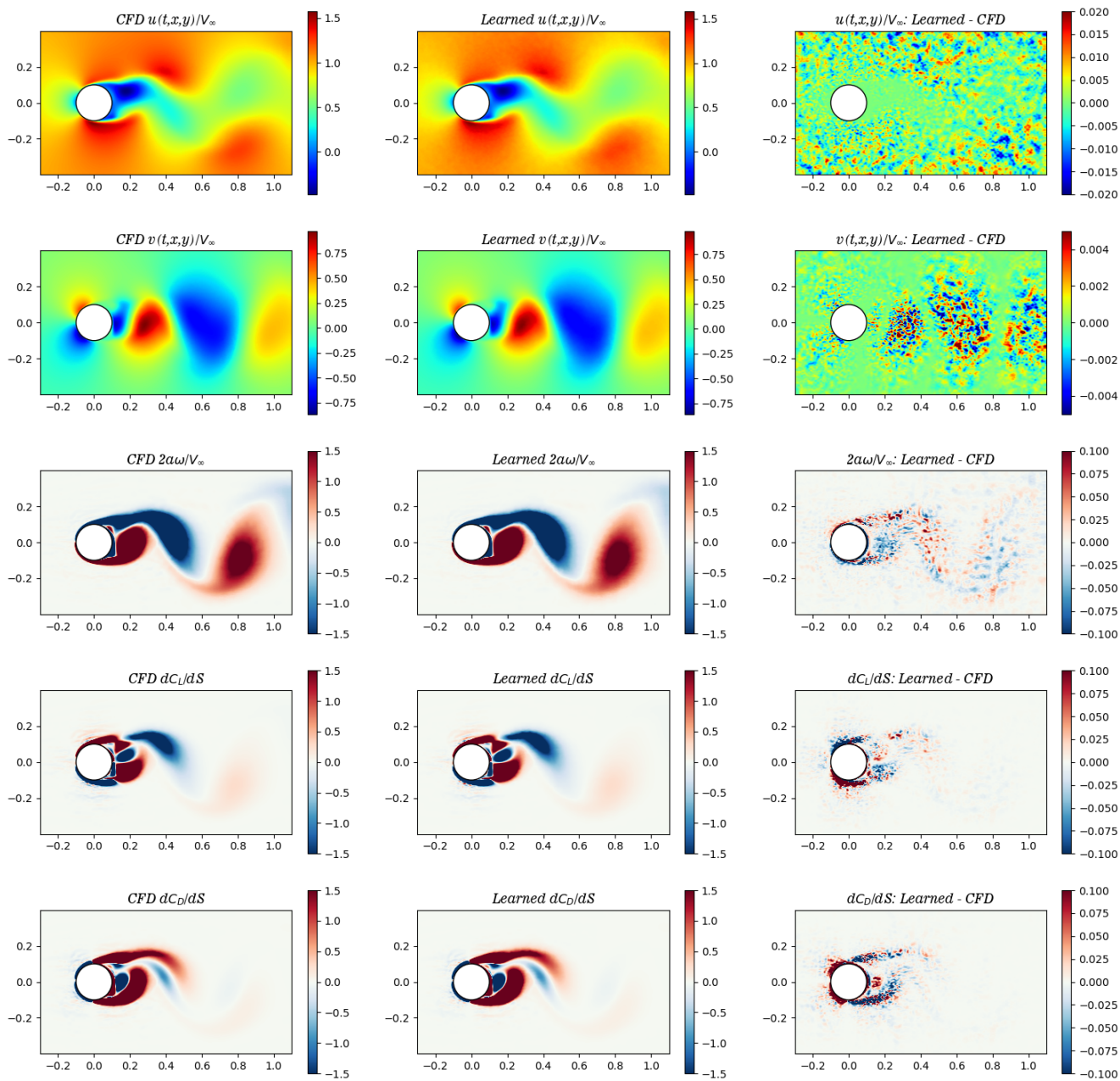


FIG. 5. The comparison of the predicted, CFD, and there differences ($\text{Learned} - \text{CFD}$) on the velocity field ($u(t,x,y)/V_\infty, v(t,x,y)/V_\infty$), the vorticity field, and the lift and drag distributions for the case of $Re = 1000$.

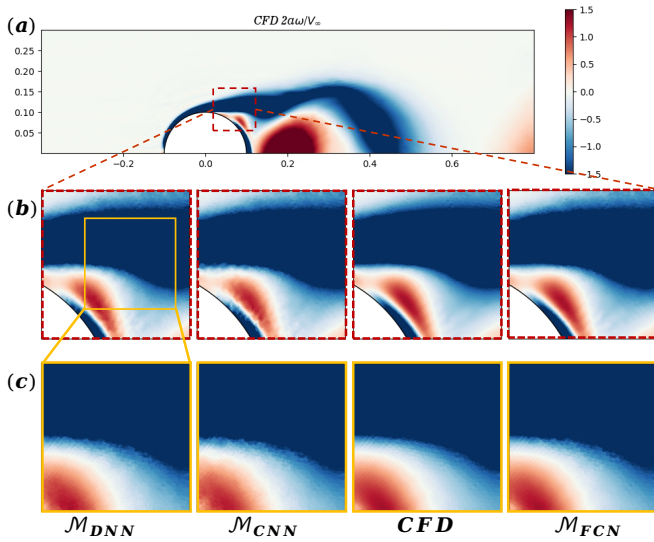


FIG. 6. The super-resolution flow field comparison of \mathcal{M}_{DNN} , \mathcal{M}_{CNN} , CFD and \mathcal{M}_{FCN} for the cylinder dataset ($Re = 1000$).

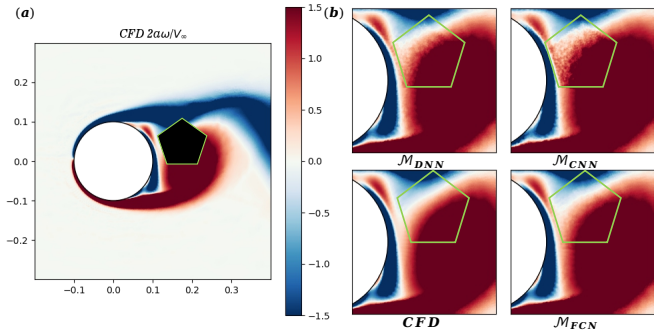


FIG. 7. The completion flow field for the cylinder dataset ($Re = 1000$) obtained from \mathcal{M}_{DNN} , \mathcal{M}_{CNN} , CFD and \mathcal{M}_{FCN} . The black pentagonal area in Fig. (a) is the flow field region that needs to be completed.

ity of our FCN model in predicting the flow field feature and body force from incomplete flow measurements on unstructured mesh or scattered points. The efficiency and accuracy of the proposed FCN model were less affected by decreasing the training dataset, and even 10% of the whole dataset gave a reasonable prediction with a 0.0546 normalized mean squared error in the test dataset. The well-designed network and variable loss functions made the model being trained quickly and robustly.

In summary, a novel neural network FCN has been proposed in this work to infer the fluid dynamics, including the flow field and the force acting on the body, from the incomplete data based on the graph convolution attention network. The FCN was designed to be capable of dealing with both structured data and unstructured data. The experimental results showed that our FCN model effectively utilizes the existing flow field information and the gradient information simultaneously, giving a better prediction of the flow field and body force than the traditional CNN-based and DNN-based

models.

ACKNOWLEDGMENTS

This work has received funding from the European Union's Horizon 2020 research and innovation programme under the Marie Skłodowska-Curie grant agreement No.765579. This work is funded by the Leverhulme Trust, Grant Ref ECF-2018-727. Their support is gratefully acknowledged.

DATA AVAILABILITY STATEMENT

The data that support the findings of this study are available from the corresponding author upon reasonable request.

- ¹C. Lagemann, K. Lagemann, S. Mukherjee, and W. Schröder, "Deep recurrent optical flow learning for particle image velocimetry data," *Nature Machine Intelligence* **3**, 641–651 (2021).
- ²X. Wen, Z. Li, D. Peng, W. Zhou, and Y. Liu, "Missing data recovery using data fusion of incomplete complementary data sets: A particle image velocimetry application," *Physics of Fluids* **31**, 025105 (2019), <https://doi.org/10.1063/1.5079896>.
- ³J. Zhang and X. Zhao, "Spatiotemporal wind field prediction based on physics-informed deep learning and lidar measurements," *Applied Energy* **288**, 116641 (2021).
- ⁴K. Fukami, R. Maulik, N. Ramachandra, K. Fukagata, and K. Taira, "Global field reconstruction from sparse sensors with voronoi tessellation-assisted deep learning," *Nature Machine Intelligence* **3**, 945–951 (2021).
- ⁵K. Ramesh, A. Gopalarathnam, K. Granlund, M. V. Ol, and J. R. Edwards, "Discrete-vortex method with novel shedding criterion for unsteady aerofoil flows with intermittent leading-edge vortex shedding," *Journal of Fluid Mechanics* **751**, 500–538 (2014).
- ⁶J. Li and Z. N. Wu, "A vortex force study for a flat plate at high angle of attack," *Journal of Fluid Mechanics* **801**, 222–249 (2016).
- ⁷A. C. Devoria, Z. R. Carr, and M. J. Ringuette, "On calculating forces from the flow field with application to experimental volume data," *Journal of Fluid Mechanics* **749**, 297–319 (2014).
- ⁸J. C. Wu, "Theory for aerodynamic force and moment in viscous flows," *AIAA Journal* **19**, 432–441 (1981).
- ⁹F. Noca, "On the evaluation of instantaneous fluid - dynamic forces on a bluff body," GALCIT Report FM96-5 (1996).
- ¹⁰C. C. Chang, "Potential flow and forces for incompressible viscous flow," *Proceedings of the Royal Society of London. Series A: Mathematical and Physical Sciences* **437**, 517–525 (1992).
- ¹¹M. S. Howe, "On the force and moment on a body in an incompressible fluid, with application to rigid bodies and bubbles at high reynolds numbers," *Quarterly Journal of Mechanics and Applied Mathematics* **48**, 401–425 (1995).
- ¹²L. L. Kang, L. Q. Liu, W. D. Su, and J. Z. Wu, "Minimum-domain impulse theory for unsteady aerodynamic force," *Physics of Fluids* **30**, 016107 (2018).
- ¹³J. Li and Z. N. Wu, "Vortex force map method for viscous flows of general airfoils," *Journal of Fluid Mechanics* **836**, 145–166 (2018).
- ¹⁴J. Li, Y. Wang, M. Graham, and X. Zhao, "Evaluating unsteady fluid dynamic forces in viscous flows from the vorticity field," *AIAA Journal* **59**, 22–33 (2021), <https://doi.org/10.2514/1.J059575>.
- ¹⁵J. Li, X. Zhao, and M. Graham, "Vortex force maps for three-dimensional unsteady flows with application to a delta wing," *Journal of Fluid Mechanics* **900**, A36 (2020).
- ¹⁶R. Maulik, K. Fukami, N. Ramachandra, K. Fukagata, and K. Taira, "Probabilistic neural networks for fluid flow surrogate modeling and data recovery," *Phys. Rev. Fluids* **5**, 104401 (2020).
- ¹⁷S. Cai, S. Zhou, C. Xu, and Q. Gao, "Dense motion estimation of particle images via a convolutional neural network," *Experiments in Fluids* **60**, 1432–1114 (2019).

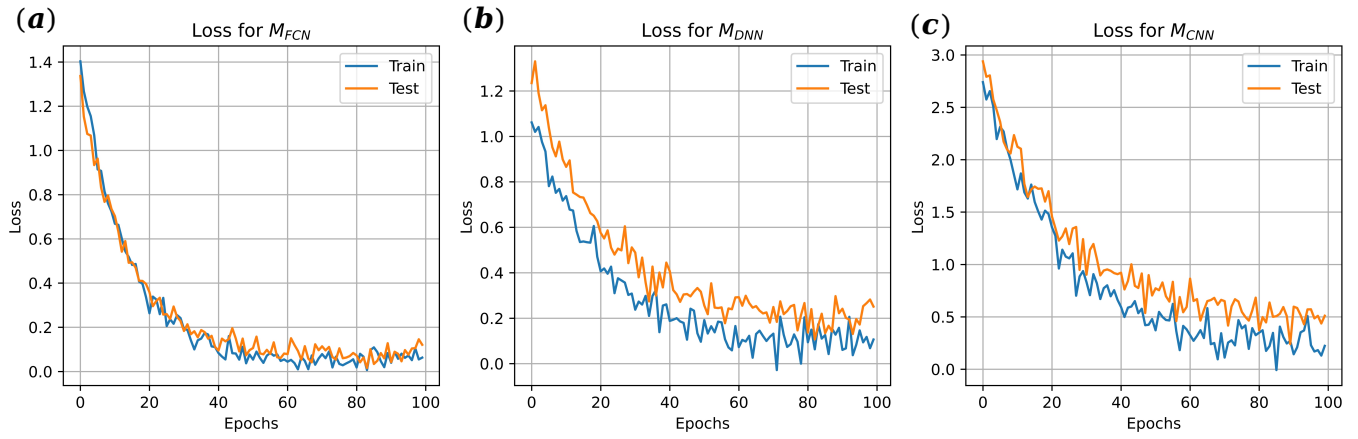


FIG. 8. The training loss and testing loss during the training procedure for (a) the proposed FCN model; (b) the CNN-based model; and (c) the DNN-based model.

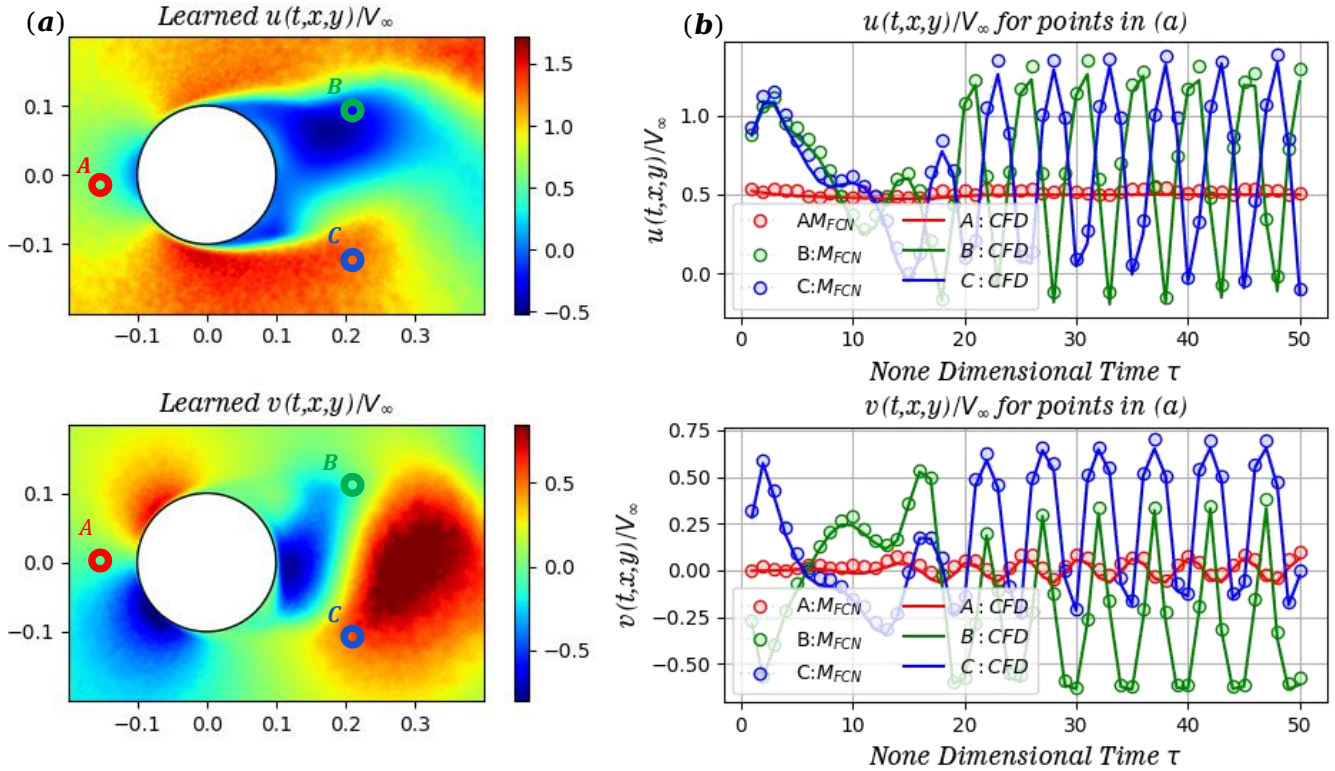


FIG. 9. The flow field completion results for (a) the velocity contours ($u/V_\infty, v/V_\infty$) at a typical instant and (b) the time variation of velocity ($u/V_\infty, v/V_\infty$) at specific points A, B, C obtained by the FCN model.

¹⁸K. Fukami, K. Fukagata, and K. Taira, “Super-resolution reconstruction of turbulent flows with machine learning,” *Journal of Fluid Mechanics* **870**, 106–120 (2019).

¹⁹M. Morimoto, K. Fukami, and K. Fukagata, “Experimental velocity data estimation for imperfect particle images using machine learning,” *Physics of Fluids* **33**, 087121 (2021), <https://doi.org/10.1063/5.0060760>.

²⁰D. Kochkov, J. A. Smith, A. Alieva, Q. Wang, M. P. Brenner, and S. Hoyer, “Machine learning–accelerated computational fluid dynamics,” *Proceedings of the National Academy of Sciences* **118** (2021), [10.1073/pnas.2101784118](https://doi.org/10.1073/pnas.2101784118),

<https://www.pnas.org/content/118/21/e2101784118.full.pdf>.

²¹M. Raissi, Z. Wang, M. Triantafyllou, and G. Karniadakis, “Deep learning of vortex-induced vibrations,” *Journal of Fluid Mechanics* **861**, 119–137 (2019).

²²M. Raissi, A. Yazdani, and G. E. Karniadakis, “Hidden fluid mechanics: Learning velocity and pressure fields from flow visualizations,” *Science* **367**, 1026–1030 (2020).

²³T. P. Miyanawala and R. Jaiman, “An efficient deep learning technique for the navier-stokes equations: Application to unsteady wake flow dynamics,” *arXiv: Fluid Dynamics* (2017).

- ²⁴S. Bhatnagar, Y. Afshar, S. Pan, K. Duraisamy, and S. Kaushik, "Prediction of aerodynamic flow fields using convolutional neural networks," *Computational Mechanics* **64**, 1432–0924 (2019).
- ²⁵N. Trask, R. G. Patel, P. J. Atzberger, and B. J. Gross, "Gmls-nets: A machine learning framework for unstructured data," in *AAAI Spring Symposium: MLPS* (2020).
- ²⁶F. Ogoke, K. Meidani, A. Hashemi, and A. B. Farimani, "Graph convolutional networks applied to unstructured flow field data," *Machine Learning: Science and Technology* **2**, 045020 (2021).
- ²⁷W. Hamilton, Z. Ying, and J. Leskovec, "Inductive representation learning on large graphs," in *Advances in Neural Information Processing Systems*, Vol. 30, edited by I. Guyon, U. V. Luxburg, S. Bengio, H. Wallach, R. Fergus, S. Vishwanathan, and R. Garnett (Curran Associates, Inc., 2017).
- ²⁸N. Wandel, M. Weinmann, M. Neidlin, and R. Klein, "Spline-pinn: Approaching pdes without data using fast, physics-informed hermite-spline cnns," (2021).
- ²⁹Q. Li, Z. Han, and X. M. Wu, "Deeper insights into graph convolutional networks for semi-supervised learning," (2018).
- ³⁰W. Huang, R. Y. T. Xu, F. Sun, and J. Huang, "Tackling over-smoothing for general graph convolutional networks," (2020).
- ³¹C. Cai and Y. Wang, "A note on over-smoothing for graph neural networks," (2020).
- ³²C. Yang, R. Wang, S. Yao, S. Liu, and T. Abdelzaher, "Revisiting over-smoothing in deep gcns," (2020).
- ³³D. Chen, Y. Lin, W. Li, P. Li, Z. J., and X. Sun, "Measuring and relieving the over-smoothing problem for graph neural networks from the topological view," (2019).
- ³⁴J. Hu, L. Shen, S. Albanie, G. Sun, and E. Wu, "Squeeze-and-excitation networks," *IEEE Transactions on Pattern Analysis and Machine Intelligence* **42**, 2011–2023 (2020).
- ³⁵K. He, X. Zhang, S. Ren, and J. Sun, "Deep residual learning for image recognition," in *2016 IEEE Conference on Computer Vision and Pattern Recognition (CVPR)* (2016) pp. 770–778.
- ³⁶R. Gao and K. Grauman, "On-demand learning for deep image restoration," in *ICCV* (2017).
- ³⁷V. Badrinarayanan, A. Kendall, and R. Cipolla, "Segnet: A deep convolutional encoder-decoder architecture for image segmentation," *IEEE Transactions on Pattern Analysis and Machine Intelligence* , 1–1 (2017).
- ³⁸J. Rabault and A. Kuhnle, "Accelerating deep reinforcement learning strategies of flow control through a multi-environment approach," *Physics of Fluids* **31**, 094105 (2019).
- ³⁹D. Liang, Y. Wang, L. Yang, W. Fang, and L. Jie, "A cnn-based vortex identification method," *Journal of Visualization* **22** (2018).
- ⁴⁰J. Cao, D. J. Farnham, and U. Lall, "Spatial-temporal wind field prediction by artificial neural networks," *CoRR* **abs/1712.05293** (2017), 1712.05293.
- ⁴¹W. L. Hamilton, R. Ying, and J. Leskovec, "Inductive representation learning on large graphs," in *Proceedings of the 31st International Conference on Neural Information Processing Systems* (2017) pp. 1025–1035.
- ⁴²V. Jayalakshmi, K. Lakshmi, and A. R. M. Rao, "Dynamic force reconstruction techniques from incomplete measurements," *Journal of Vibration and Control* **24**, 5321–5344 (2018), <https://doi.org/10.1177/1077546317752709>.